SCIENTIFIC REPORTS

OPEN

SUBJECT AREAS:
NANOPHOTONICS AND PLASMONICS
IMAGING AND SENSING
BIOMEDICAL MATERIALS

Received
16 May 2014

Accepted
12 September 2014

Published
9 October 2014

Correspondence and requests for materials should be addressed to M.C.T. (meichee.tan@sutd.edu.sg)

Rare-Earth Doped Particles as Dual-Modality Contrast Agent for Minimally-Invasive Luminescence and Dual-Wavelength Photoacoustic Imaging

Yang Sheng[1], Lun-De Liao[2], Nitish Thakor[2,3,4] & Mei Chee Tan[1]

[1]Engineering Product Development, Singapore University of Technology and Design, Singapore, 20 Dover Drive, Singapore 138682, [2]Singapore Institute for Neurotechnology (SINAPSE), National University of Singapore, 28 Medical Drive, #05-COR, Singapore 117456, [3]Department of Biomedical Engineering, Johns Hopkins University, Traylor 701/720 Rutland Ave, Baltimore, MD 21205, U.S.A, [4]Department of Electrical and Computer Engineering, and Department of Bioengineering, National University of Singapore, Singapore 117456.

Multi-modal imaging is an emerging area that integrates multiple imaging modalities to simultaneously capture visual information over many spatial scales. Complementary contrast agents need to be co-developed in order to achieve high resolution and contrast. In this work, we demonstrated that rare-earth doped particles (REDPs) can be employed as dual-modal imaging agents for both luminescence and photoacoustic (PA) imaging to achieve intrinsic high contrast, temporal and spatial resolution, reaching deeper depth. REDPs synthesized with different surfactants (citric acid, polyacrylic acid, ethylenediaminetetraacetic acid and sodium citrate) exhibit tunable emission properties and PA signal amplitudes. Amongst these samples, sodium citrate-modified REDPs showed the strongest PA signals. Furthermore, since REDPs have multiple absorption peaks, they offer a unique opportunity for multi-wavelength PA imaging (e.g. PA signals were measured using 520 and 975 nm excitations). The *in vivo* PA images around the cortical superior sagittal sinus (SSS) blood vessel captured with enhanced signal arising from REDPs demonstrated that in addition to be excellent luminescent probes, REDPs can also be used as successful PA contrast agents. Anisotropic polyacrylic acid-modified REDPs were found to be the best candidates for dual-modal luminescence and PA imaging due to their strong luminescence and PA signal intensities.

Imaging techniques have been used to visualize biochemical pathways in healthy and diseased states, and characterize structure-function relationships at the cellular, tissue and anatomical levels. Although imaging techniques have been useful for monitoring dynamic physiological processes over time, achieving both the resolution (i.e. both temporal and spatial) and the signal-to-noise ratio (SNR) remain a challenge for noninvasive functional imaging techniques. Therefore, together with the design of innovative imaging modalities, complementary imaging probes or contrast agents are continually being co-developed to improve the resolution and the SNR. An emergent technological development is multi-modal imaging that integrates multiple imaging modalities with compatible contrast agents to simultaneously capture visual information over many spatial scales at high SNR[1–3]. The combination of complementary imaging techniques offers attractive outcomes, such as: (1) cooperative synergy of the strengths for individual modality, (2) reduce data processing time with the co-registration of multiple signals instead of obtaining sequential images of independent modality, and (3) reduce exposure risks and inconvenience undertaken by subjects with a one-time contrast agent injection.

Many of the current efforts have been directed towards developing multi-modal systems which involves the integration of one or more of the following: X-ray computed tomography (CT), magnetic resonance imaging (MRI), positron emission tomography (PET), optical coherence tomography (OCT, optical), luminescence imaging (optical) and photoacoustic (PA) imaging[4–7]. For clinical applications, the use of high ionizing radiation sources (e.g., X-rays) or expensive, time-consuming methods (e.g., MRI) lead to less favorable risk-benefit or cost-benefit ratios. The successful integration of an all optical-based imaging multi-modality platform presents a unique approach for a non-invasive and inexpensive intraoperative system that can be easily adapted for surgical guidance[8].

Luminescence imaging is a well-established, fast visualization technique, which can be easily adapted using portable devices and an extensive library of available fluorophores for real-time surgical guidance[2,9,10]. Despite

having excellent temporal response and high sensitivity, some of the drawbacks of luminescence imaging operating in the UV and visible spectral range are relatively low spatial resolution and limited penetration depth due to attenuation of light by the tissue. Recently, it was shown that anatomical features (e.g. spleen, lung, blood vessels) located up to ~1 cm beneath the skin can be resolved by using short wavelength infrared (SWIR) imaging where the tissue attenuation is lower compared to UV and visible light[9]. In contrast, penetration depths of up to 5 cm can be achieved by using an emerging novel optical imaging modality known as PA imaging[11–16]. PA imaging converts laser energy at a specific wavelength into acoustic waves that can be detected using ultrasound. PA imaging can be used to image tissues with a high spatial resolution, and with a better contrast at deeper penetration depth because ultrasound scattering is two to three orders of magnitude weaker than UV and visible optical scattering in tissues[17]. The SNR of PA imaging can be improved by employing exogenous contrast agents to enhance the acoustic signal and utilizing excitation sources in the near infrared (NIR) region to minimize tissue attenuation[18]. Furthermore, exogenous contrast agents facilitate identification of disease states since the PA signal from some diseased tissues (e.g. early stage tumors, cerebral cortex, etc.) is indistinct and weak[19,20]. By combining luminescence and PA imaging modalities, a single, versatile minimally-invasive imaging platform can be designed to enable visualization for deep tissue diagnostics and potential real-time surgical guidance. Whilst there have been a few recent reports using gold nanoparticles and quantum dots for PA imaging, the clinical translation of these materials has been limited due to various issues, including the lack of absorption tunability and cytotoxicity[21–23]. Therefore, it is very important to establish new contrast agents that: (1) have optical properties that can be easily tuned, (2) have low cytotoxicity, and (3) are able to enhance the signals for both luminescence and PA imaging[24].

Rare-earth doped particles (REDPs) are well-established as luminescent biomarkers because they exhibit low cytotoxicity and sharp absorption and emission peaks spanning the entire visible and infrared region which can be precisely tuned by changing the RE^{3+} dopant and host chemistries for particles of any size[2,25–28]. To date, REDPs have been developed to combine luminescence imaging with X-ray computed tomography (CT)[29,30], magnetic resonance imaging (MRI)[31,32], or positron emission tomography (PET)[33,34]. In this work, we seek to demonstrate that REDPs can be used for both luminescence and PA imaging. Compared with other potential PA contrast agents, REDPs offer advantages of highly controllable absorption behavior and low cytotoxicity[28,35]. Since the absorption behavior of REDPs are governed by the f-f transitions of the RE dopants and are consequently independent of particle size or morphology, this opens an opportunity for multi-wavelength PA imaging. Just as part of this absorbed light is converted into upconversion and downshifting luminescence emissions, another portion is converted into other energy forms including acoustic energy. Therefore, REDPs can potentially be applied for PA imaging. The PA properties of $NaYF_4$:Yb,Er particles, a well-established material with known luminescence properties[2,28], are studied here to evaluate the usefulness of REDPs for dual modality imaging. $NaYF_4$:Yb,Er of different morphologies coated with different surfactants are prepared using the hydrothermal method and systematically characterized for their physical properties (e.g., size, morphology, crystal structure)[27]. In addition, *in vivo* tests are conducted to evaluate the feasibility using $NaYF_4$:Yb,Er particles as a PA contrast agent.

Results

Preparation and Physical Characterization of REDPs. Micron-sized $NaYF_4$:Yb,Er particles with various morphologies were prepared via the hydrothermal approach[27]. The morphology and size of the particles were controlled by four different surface capping agents: citric acid, ethylenediaminetetraacetic acid (EDTA), polyacrylic acid (PAA), and sodium citrate, where "citric acid-modified", "EDTA-modified", "PAA-modified" and "sodium citrate-modified" are labels used strictly for the purpose of sample identification. Figure 1 shows the SEM images of $NaYF_4$:Yb,Er particles (Ln:Surf = 1 : 10 mol/mol) with aspect ratios ranging from 1 to 5.5 (see Supplementary Fig. S1, aspect ratio = major: minor axes) and particle diameters ranging from 200 to 500 nm. Amongst these samples, PAA-modified particles exhibited the highest aspect ratio and degree of anisotropy, while sodium citrate-modified particles were mostly isotropic. The different particle morphologies were controlled by modifying the binding affinity of surfactants to specific crystals planes leading to the preferential growth of some planes at the expense of others[36,37]. The particle sizes were also tuned by varying the molar ratio of RE ions to surfactants (see Supplementary Fig. S2 to S5). Figure 2 shows the X-ray diffraction (XRD) profiles of the four samples, which confirms that hexagonal phase $NaYF_4$:Yb,Er were synthesized. Using the Scherrer equation, the calculated grain size for the as-synthesized $NaYF_4$:Yb,Er particles are similar and range from 40 to 60 nm. Therefore, both the XRD and SEM results showed that polycrystalline, hexagonal phase sub-micron REDPs were prepared. The difference in intensity ratios between the (110) and (101) planes for the four samples supports our earlier observations from the SEM micrographs that PAA, EDTA and citric acid-modified particles exhibit anisotropic properties whilst that sodium citrate-modified particles show an isotropic behavior. In addition, by comparing the XRD intensity ratios, the PAA-modified particles exhibited the highest degree of anisotropy which was consistent with the SEM observations.

Absorption and Luminescence Properties of REDPs. To demonstrate that the as-synthesized $NaYF_4$:Yb,Er particles exhibit the characteristic up-conversion and downshifting luminescence behavior, we measured the absorption and emission spectra as shown in Figures 3A and 3B. The two strongest absorption peaks are found at 520 and 976 nm, where the absorbance at 976 nm is approximately ~4 times of that of 520 nm. Since these REDPs absorb at many wavelengths with narrow bandwidths, multiple excitation sources can be used for PA imaging. Figure 3B shows the characteristic steady state visible and IR emissions of a typical as-synthesized NaYF4:Yb,Er particles upon 975 nm excitation, due to the resonant transfer of excitation energy from the sensitizer (Yb) to the activator (Er)[10]. Whilst the visible upconversion emissions occur through non-linear optical processes, the IR downshifting emission is a linear optical process[26]. Therefore, the 1530 nm IR emission properties corresponding to the $^4I_{13/2} \rightarrow {}^4I_{15/2}$ transition were studied to compare the contribution of non-radiative losses that will be proportional to the PA intensity.

Figure 3C shows the steady state IR emission properties of our REDPs. Sodium citrate-modified REDPs showed the lowest IR emission intensity, which was ~2.5 times lower than that of citric acid-modified particles. Considering that the particle sizes were in the sub-micron regime, surface quenching effects on the emission intensity would be negligible for these particles[38]. Therefore, the observed difference in emission intensities is most likely due to different particle morphologies. The low emission intensity of sodium citrate-modified particles also indicates that more of the absorbed energy was converted into non-radiative forms compared to the other three samples.

Next, to study the non-radiative characteristics of these samples, time-resolved spectroscopy was used to measure the luminescence decay time of the 1530 nm emission. Figure 3D shows the measured decay curves of the samples upon excitation at 975 nm. The decay curves were next fitted to a first-order exponential function to obtain the lifetimes, τ. Lifetimes of 125, 449, 507 and 714 μs were estimated for sodium citrate-, citric acid-, EDTA- and PAA-modified particles,

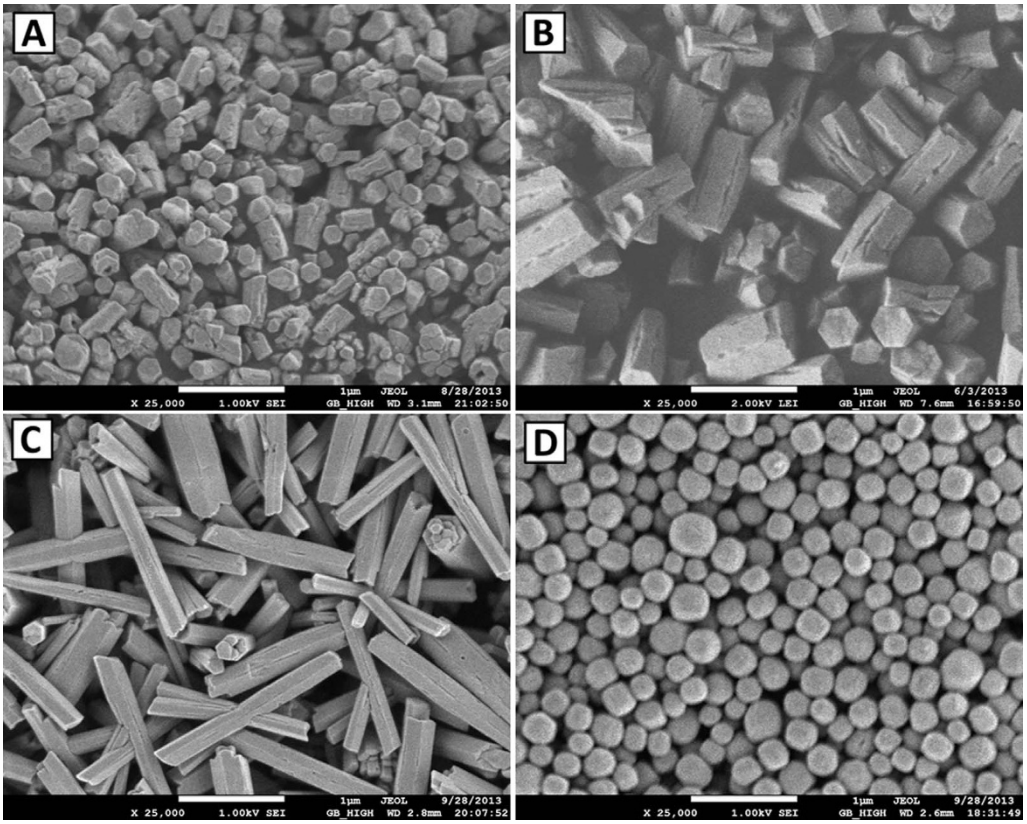

Figure 1 | SEM images of $NaYF_4$:Yb,Er particles synthesized by hydrothermal method using different surfactants of (A) citric acid, (B) EDTA, (C) PAA and (D) sodium citrate (Ln: Surf = 1 : 10 mol/mol). (Scale bar: 1 μm).

respectively. In general, long lifetime is an indicator for bright emissions, low non-radiative losses, and high internal quantum efficiency. Therefore, based on the estimated lifetimes we would expect the PA signals from sodium citrate-modified particles to be the strongest (shortest τ, most non-radiative losses) and PAA-modified particles to be the weakest (longest τ, least non-radiative losses).

PA Signals from REDPs Using Dual-wavelength Excitation. To evaluate the PA properties of our REDPs and demonstrate dual-wavelength excitation for PA imaging, PA signals of our REDPs that were injected into polyethylene tubings were measured using a dark-field confocal photoacoustic microscopy (PAM) system upon excitation at 520 and 975 nm. Figure 4 shows that PA signals were obtained from our samples at a concentration of 33.3 mg/mL using both 520 nm and 975 nm excitation. Although the absorption spectrum in Figure 3A shows that the absorbance of our REDPs at 520 nm is ~4 times lower than that at 976 nm, the PA signals obtained using both excitation wavelengths were comparable. This is due to the non-linear relationship between the amplitude of the PA signal and absorption coefficient[39]. This non-linear relationship was verified by studying the dependence of the PA signal on the concentration using the sodium citrate-modified REDPs which generated the strongest PA signal (see Fig. 5A and 5B). Consistent with the literature findings, a non-linear logarithmic relationship between the PA signal amplitude and REDP concentration was observed ($R^2 = 0.97$)[39]. In addition, the sodium citrate-modified REDPs showed the highest PA amplitude of 0.91, while the PAA-modified REDPs which showed an intense IR emission surprisingly exhibited a relatively strong PA signal of 0.84. A possible explanation for the strong PA signal and intense IR emission of PAA-modified REDPs is that the high degree of anisotropy and large aspect ratio have influenced PA generation or transmission from the REDPs. PA signals are affected by multiple parameters: optical, thermal, elastic and geometrical[39]. Since all samples are the same material of $NaYF_4$:Yb,Er, their optical absorption, thermal and elastic coefficients are identical to each other, while the geometrical parameter is determined by their different size and aspect ratio. Therefore, although PAA-modified REDPs displayed high luminescence intensity, the high aspect ratio is a possible explanation for the observed high PA signals.

To further reinforce the feasibility of REDPs for biomedical PA imaging, the PA images of nano-sized $NaYF_4$:Yb,Er/$NaYF_4$ particles were collected and a signal amplitude of 0.31 was measured using a PAM system upon excitation at 975 nm (see Supplementary Figure S7). The results showed that PA signals were also generated from nano-sized REDPs. Compared to the sub-micron REDPs, the PA signals from the nano-sized REDPs were weaker by about 2 to 3 times. There are many possible causes (e.g., size, shape, surface ligand functional groups, surface quenching) for the difference in PA intensity. A separate study is needed to obtain a comprehensive understanding of these effects, which is not within the scope of this manuscript.

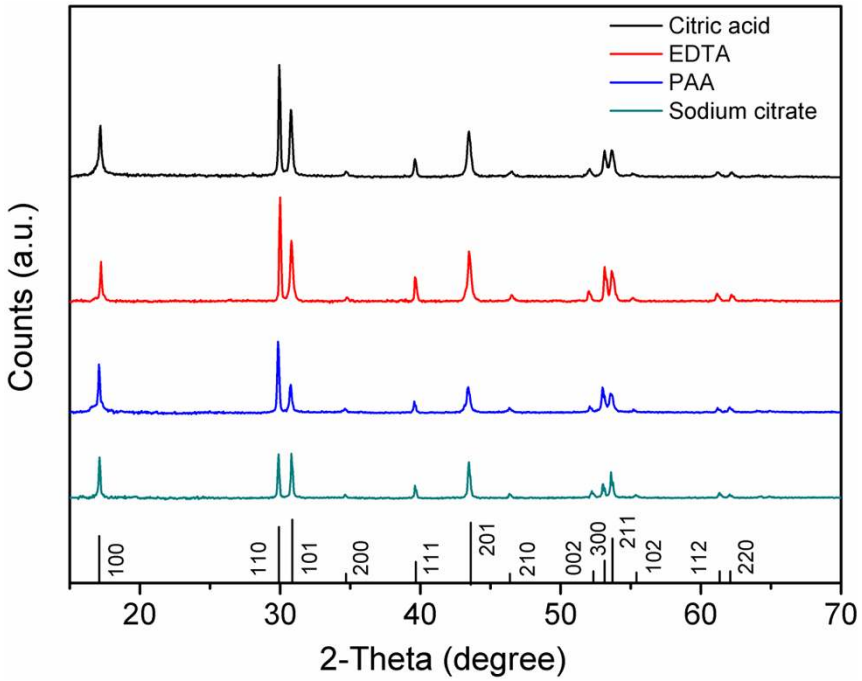

Figure 2 | XRD patterns of $NaYF_4$:Yb,Er particles with diffraction peaks assigned to the hexagonal phase (PDF no. 16-0334). Intensity ratios of the (110) to (101) planes for reference, citric acid-, EDTA-, PAA- and sodium citrate-modified REDPs are 1 : 1.13, 1 : 0.60, 1 : 0.58, 1 : 0.39 and 1 : 1.02, respectively.

***In Vivo* PA Imaging of REDPs.** To demonstrate the feasibility of our REDPS for *in vivo* PA imaging, sodium citrate-modified REDPs were injected into the blood vessel of the rat's brain around the superior sagittal sinus (SSS) and monitored with a PAM system upon excitation at 975 nm. The benefit of using the 975 nm excitation is that deeper penetration depths can be reached since tissue attenuation in the infrared region is low. The PA signal was monitored for ~30 min after administration of REDPs (Fig. 5C and 5D, and Supplementary Fig. S6). The background signal from blood absorption was detected to be ~0.27 before the injection. The PA signal amplitude readily increased to ~0.73 at 10 minutes after injection, which was ~2.5 times of the background signal. The PA signal amplitude was observed to decrease slowly over the following 20 min to 0.46, which indicates good blood circulation of REDPs. The obvious signal enhancement from our REDPs at 10 min mark and clear differentiation of the blood vessel around the SSS over ~20 min time demonstrated the usefulness of our REDPs as PA contrast agent. The key objective of the *in vivo* experiment is to demonstrate that a PA signal contrast was detected and measured upon excitation of the REDPs at 975 nm. It should be noted that further optimization (e.g. particle surface modification to reduce surface quenching, excitation wavelength to penetrate deeper) is required for the eventual application of these materials.

Discussion

In this work, we have demonstrated for the first time that REDPs can also be applied for PA imaging. The PA signal enhancement arising from our REDPs and clear differentiation of the rat's blood vessels around the SSS demonstrated the usefulness of our REDPs as a PA contrast agent, in addition to being excellent luminescent probes. Therefore, these REDPs can be used as a contrast agent for a minimally-invasive luminescence-photoacoustic dual modality imaging platform. Rather than considering the non-radiative losses as an undesirable attribute, our work shows how this lost energy is harnessed to generate useful PA signals.

Luminescence and PA signals are complementary signal forms which result from radiative and non-radiative relaxations of electrons, respectively. Therefore it is usually expected that materials exhibiting bright luminescence emissions would have weak PA signals, whilst weak luminescence emissions would be accompanied by strong PA signals[22]. Here, we have found that PAA-modified REDPs exhibited both relatively bright luminescence emissions and strong PA signals[40]. The high aspect ratio of PAA-modified REDPs is a possible explanation for the observed high PA signals. Hence, although sodium citrate-modified REDPs showed the highest PA signals, PAA-modified REDPs which showed both strong luminescence and PA signals are the best contrast agent for a dual modality luminescence-PA imaging platform.

In this study, both 520 and 975 nm excitations were used to generate PA signals from our REDPs for demonstration of dual-wavelength PA imaging. Since the multiple absorption peaks of REDPs (see Fig. 3A) are due to the RE f-f transitions, the absorption peak positions are thus insensitive to the particle morphology and surface characteristics. Therefore, compared to other existing PA contrast agents, it is possible to study the effects of different morphologies on PA generation and transmission. Furthermore, since the absorption peak positions and intensities are precisely controlled by RE dopant choices and concentrations, REDPs with different absorption wavelengths (e.g., $NaYF_4$:Yb,Tm with 800 nm absorption[41], see Supplementary Fig. S8 for PA signal) are conveniently produced by changing the dopants while keeping particle size and morphology unchanged. This potential ability to design REDPs with precisely tunable absorption and PA properties presents an untapped opportunity to develop a library of PA contrast agents that can be excited with different wavelengths whilst also controlling PA signal generation.

In summary, we have shown the first demonstration of REDPs as contrast agents to enhance resolution and SNR for dual-modality luminescence-PA imaging. Both the radiative and non-radiative relaxations were exploited to obtain luminescence and PA contrast signals at the same time by using a single excitation wavelength in the infrared tissue penetrating region of the REDPs. Our results show that sodium citrate-modified REDPs have the highest PA signals while the anisotropic PAA-modified REDPs in the form of rods are the best candidate for dual-modality luminescence-PA imaging.

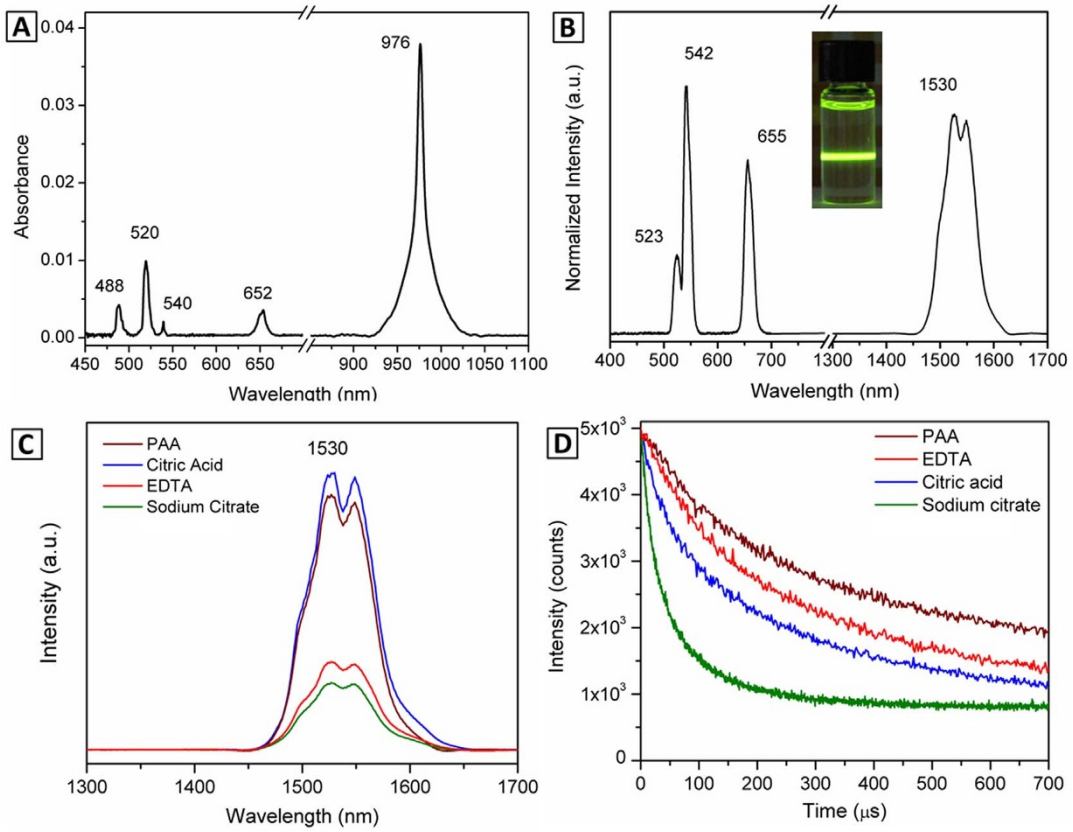

Figure 3 | (A) Absorption spectrum of sodium citrate-modified $NaYF_4$:Yb,Er particles (Ln:Surf = 1 : 10 mol/mol). The five absorption peaks of 488, 520, 540, 652, and 976 nm correspond to the f-f transition of $^4F_{7/2}$ (Er^{3+}), $^4H_{11/2}$ (Er^{3+}), $^4S_{3/2}$(Er^{3+}), $^4F_{9/2}$ (Er^{3+}), and $^4F_{5/2}$ (Yb^{3+}) + $^4I_{11/2}$ (Er^{3+}) states. (B) Characteristic steady state luminescence spectrum of $NaYF_4$:Yb,Er particles spanning visible and IR range. The line break in the x-axis is due to the use of 2 different detectors required to measure the emissions in the visible (400 to 800 nm) and infrared regions (1000 to 1700 nm). Inset: photograph of $NaYF_4$:Yb,Er sample dispersed in dimethyl sulfoxide illuminated with a hand held 975 nm laser pen at ~400 mW. (C) Steady-state and (D) time-resolved luminescence spectra of $NaYF_4$:Yb,Er particles (Ln: Surf = 1 : 10 mol/mol) corresponding to the $^4I_{13/2}$–$^4I_{15/2}$ transition of Er^{3+} at 1530 nm.

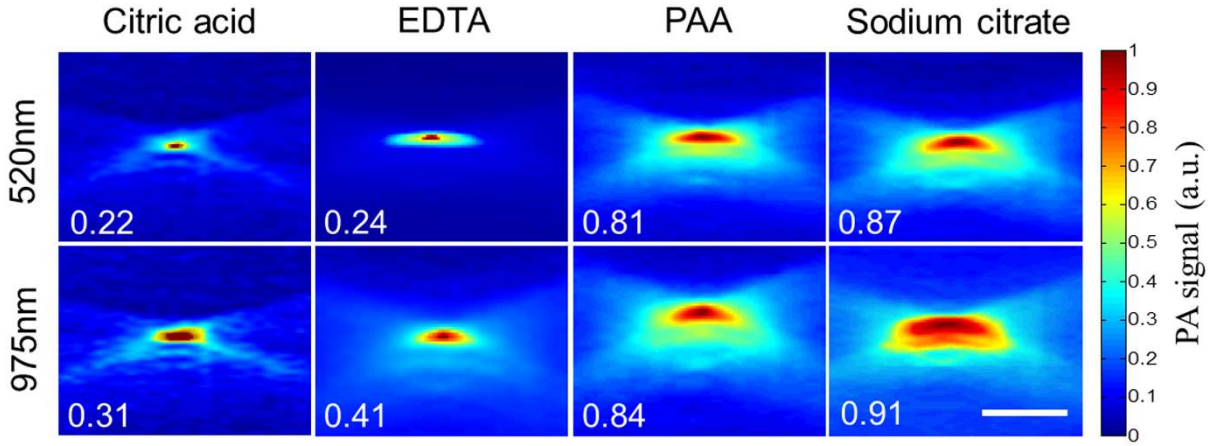

Figure 4 | **The PA images and signals measured using 520 and 975 nm excitation sources for four samples synthesized using citric acid, EDTA, PAA and sodium citrate as surfactants, at the concentration of 33.3 mg/mL.** (Scale bar: 100 μm).

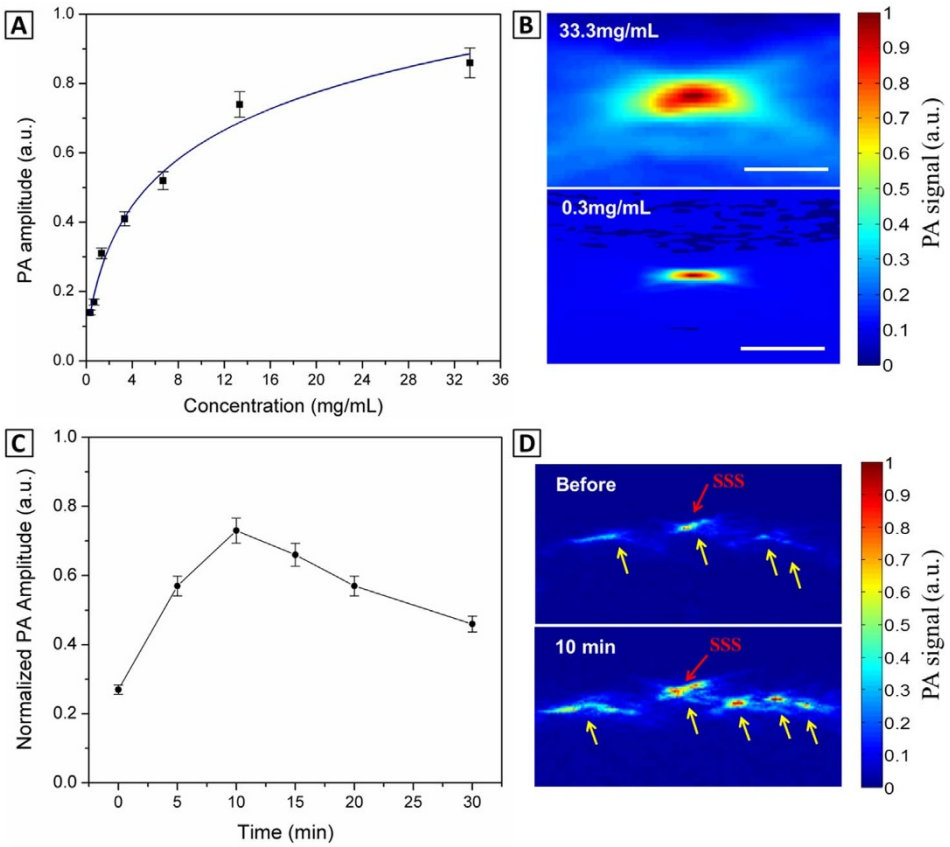

Figure 5 | (A) The measured PA signals and (B) PA images (scale bar: 100 μm) captured for sodium citrate-modified $NaYF_4$:Yb,Er particles (Ln:Surf = 1 : 10 mol/mol) injected into polyethylene micro tubing at different concentrations. (C) The PA signal of sodium citrate-modified $NaYF_4$:Yb,Er particles injected into the blood vessel of the rat around the SSS with respect to time. (D) The cortical PA images (includes SSS blood vessel) before and 10 min after injection of our REDPs. (Image dimension: 6 mm in width and 2.5 mm in depth).

Methods

Materials. All chemicals were purchased from manufacturers and used as obtained without any further purification. The following chemicals were used in this study. Sodium fluoride (NaF), lanthanide chloride hexahydrate (99.99%, $YCl_3{\cdot}6H_2O$, $YbCl_3{\cdot}6H_2O$, $ErCl_3{\cdot}6H_2O$), citric acid (99.5%), ethylenediaminetetraacetic acid (EDTA, 99%), polyacrylic acid (PAA, Mw ~1800), and sodium citrate tribasic dihydrate (99%) were purchased from Sigma-Aldrich (Sigma-Aldrich, St. Louis, MO).

Preparation of $NaYF_4$:Yb,Er samples. The molar ratio between lanthanide precursors and surfactants of 1 : 1 to 1 : 10 were used to synthesize $NaYF_4$:Yb,Er particles. In a typical experiment to prepare $NaYF_4$:Yb,Er using a surfactant such as sodium citrate, 1.56 mmol $YCl_3{\cdot}6H_2O$, 0.4 mmol $YbCl_3{\cdot}6H_2O$ and 0.04 mmol $ErCl_3{\cdot}6H_2O$ were dissolved in 20 mL of H_2O. Next, 1 g of NaF and 5.88 g sodium citrate tribasic dihydrate were added into a Teflon liner together with the lanthanide chloride solution, followed by heating up to 150°C for 6 hours before cooling down to room temperature. The obtained particles were washed by centrifugation and re-dispersion in H_2O for several times. After drying in oven at 60°C, the obtained powders were ready for further characterization and imaging application.

Preparation of nano-sized $NaYF_4$:Yb,Er nanoparticles. The details of the synthesis process is discussed in our previous work[9]. Briefly, the precursors of Ln trifluoroacetate were prepared by dissolving Ln oxide powders in the presence of trifluoroacetate acid at 80°C. The core precursor solution was prepared by dissolving stoichiometric amounts of erbium trifluoroacetate, yttrium trifluoroacetate, ytterbium trifluoroacetate in oleylamine. The shell precursor solution was prepared by dissolving stoichiometric amounts of the sodium and yttrium trifluoroacetates in oleylamine. The core solution was then heated to 340°C under vigorous stirring in inert argon atmosphere to allow the formation of the core particles. The shell precursor was then added to enable the formation of core-shell particles. Upon completion of the reaction and after cooling, the synthesized nanoparticles were washed three times in ethanol by centrifuging.

Sample for PA characterization and *in vivo* animal imaging were prepared by dispersing the powders in H_2O. Various REDP concentrations from 0.3 to 33.3 mg/mL were obtained by dispersing the powder into H_2O for the concentration-dependent PA signal measurement and *in vivo* small animal imaging.

Materials Characterization. The size and morphology of the synthesized NaYF4:Yb,Er particles were characterized by field emission scanning electron microscopy (JSM-7600F, JEOL Ltd., JP). Powder XRD patterns were recorded by the D2 PHASER powder diffractometer (Bruker AXS Inc., Madison, WI) using $\lambda_{CuK\alpha}$ of 1.541 Å. Steady state luminescence spectra were measured upon excitation with a 975 nm continuous wave laser (CNI MDL-III-975, Changchun New Industries Optoelectronics Tech. Co. Ltd, China) using two different spectrometers for the visible (USB2000, Ocean Optics Inc., Newark, NJ) and NIR (NIRQuest512, Ocean Optics Inc.) ranges, respectively. Luminescence lifetime was measured using a Edinburgh Instruments spectrometer (FSP920, Edinburgh Instruments, Livingston, U.K.) equipped with a 980 laser (Changchun New Industries Optoelectronics Tech. Co, Ltd, Changchun, China) and PMT (Hamamatsu R928P, Hamamatsu Photonics K.K., Japan) and NIR-PMT (Hamamatsu R5509-72, Hamamatsu Photonics K.K., Japan).

PA Measurement. Various test samples were injected and into a ~15 cm polyethylene tubing (0.38 × 1.09 mm, Scientific Commodities, Inc, Lake Havasu

City, Arizona). Afterwards, the tubing was positioned at a depth of the transducer's focus, i.e., the depth of 9 mm with respect to the transducer in water tank. The system was maintained in a 25°C water bath throughout the experiment. The contrast changes of the REDPs were imaged using a 50-MHz dark field confocal PAM system with 32 × 61 μm resolution. An optical parametric oscillator pumped by a frequency-tripled Nd:YAG Q-switched laser was employed to provide ~4 ns laser pulses at a pulse repetition rate of 10 Hz. Laser energy was delivered by a 1 mm multimode fiber. The fiber tip was coaxially aligned with a convex lens, an axicon, a plexiglass mirror, and an ultrasonic transducer on an optical bench, forming dark field illumination that is confocal with the focal point of the ultrasonic transducer. Laser pulses at 975 nm were used for PA wave excitation. A large numerical-aperture, wideband 50-MHz ultrasonic transducer was employed to allow for the efficient collection of PA signals. The scanning step size was 20 μm for each B-scan.

The PA signals received by the ultrasonic transducer were pre-amplified by a low-noise amplifier (noise figure 1.2 dB, gain 55 dB, AU-3A-0110, Miteq, USA), cascaded to an ultrasonic receiver (5073 PR, Olympus, USA), then digitized and sampled by a computer-based 14-bit analog to digital (A/D) card (CompuScope 14200, GaGe, USA) at a 200-MHz sampling rate for data storage. Fluctuations in the laser energy were monitored by a photodiode (DET36A/M, Thorlabs, USA). Recorded photodiode signals were applied to compensate for PA signal variations caused by laser energy instability before any further signal processing. No signal averaging was performed in this study. Note that the amplitude of the envelope-detected PA signal was used in the imaging analysis.

***In Vivo* PA Brain Vascular Imaging.** The experimental setup for brain vasculature imaging using dark-field strong-focusing photoacoustic microscopy (PAM) is described in detail elsewhere[42,43]. Male Sprague Dawley rats weighing 250 to 300 g each were used for PA imaging and 1 ml of 15 mg/mL sample was used to inject into the rat. The animals were housed at a constant temperature and humidity with free access to food and water. Before the imaging experiment, the rats were fasted for 24 hours but given water ad libitum. All animal experiments were conducted in accordance with the guidelines of the Animal Research Committee of National University of Singapore. The animals were initially anesthetized with 3% isoflurane. Supplemental α-chloralose anesthesia (70 mg/kg) was injected intraperitoneally as needed. The anesthetized rats were mounted on a custom built acrylic stereotaxic head holder, and the skin and muscle were cut off to expose the bregma landmark. The anteroposterior distance between the bregma and the interaural line was surveyed directly. Furthermore, the craniotomy was performed for each animal and the bilateral cranial window with approximately 6 (horizontal) × 3 (vertical) mm size was fashioned with a high-speed drill. The interaural and bregma references were then used to position the heads in the PAM system without additional surgery in following experiments.

1. Ntziachristos, V. Going deeper than microscopy: the optical imaging frontier in biology. *Nat Meth* **7**, 603–614 (2010).
2. Naczynski, D. J., Tan, M. C., Riman, R. E. & Moghe, P. V. Rare earth nanoprobes for functional biomolecular imaging and theranostics. *J Mater Chem B* **2**, 2958–2973 (2014).
3. Kim, J., Piao, Y. & Hyeon, T. Multifunctional nanostructured materials for multimodal imaging, and simultaneous imaging and therapy. *Chem Soc Rev* **38**, 372–390 (2009).
4. Kircher, M. F. *et al.* A brain tumor molecular imaging strategy using a new triple-modality MRI-photoacoustic-Raman nanoparticle. *Nat Med* **18**, 829–834 (2012).
5. Kircher, M. F., Mahmood, U., King, R. S., Weissleder, R. & Josephson, L. A multimodal nanoparticle for preoperative magnetic resonance imaging and intraoperative optical brain tumor delineation. *Cancer Res* **63**, 8122–8125 (2003).
6. Nahrendorf, M. *et al.* Hybrid PET-optical imaging using targeted probes. *Proc Natl Acad Sci USA* **107**, 7910–7915 (2010).
7. Wang, L. V. Multiscale photoacoustic microscopy and computed tomography. *Nat Photonics* **3**, 503–509 (2009).
8. Kaijzel, E. L., van der Pluijm, G. & Lowik, C. W. G. M. Whole-body optical imaging in animal models to assess cancer development and progression. *Clin Cancer Res* **13**, 3490–3497 (2007).
9. Naczynski, D. J. *et al.* Rare-earth-doped biological composites as in vivo shortwave infrared reporters. *Nat Commun* **4** (2013).
10. Sheng, Y., Liao, L. D., Thakor, N. V. & Tan, M. C. Nanoparticles for molecular imaging. *J Biomed Nanotechnol* **10**, 2641–2676 (2014).
11. Xu, M. & Wang, L. V. Photoacoustic imaging in biomedicine. *Rev Sci Instrum* **77**, 041101 (2006).
12. Wang, P., Rajian, J. R. & Cheng, J.-X. Spectroscopic imaging of deep tissue through photoacoustic detection of molecular vibration. *J Phys Chem Lett* **4**, 2177–2185 (2013).
13. Liu, J. *et al.* Conjugated polymer nanoparticles for photoacoustic vascular imaging. *Polym Chem* **5**, 2854–2862 (2014).
14. Kong, K. V. *et al.* Organometallic carbonyl clusters: a new class of contrast agents for photoacoustic cerebral vascular imaging. *Chem Commun* **50**, 2601–2603 (2014).
15. Xiang, L., Wang, B., Ji, L. & Jiang, H. 4-D photoacoustic tomography. *Sci Rep* **3**, 1113 (2013).
16. Liao, L.-D. *et al.* Transcranial imaging of functional cerebral hemodynamic changes in single blood vessels using in vivo photoacoustic microscopy. *J Cereb Blood Flow Metab* **32**, 938–951 (2012).
17. Duck, F. A. *Physical properties of tissue: a comprehensive reference book.* (Academic Press, USA, 1990).
18. Ku, G. & Wang, L. V. Deeply penetrating photoacoustic tomography in biological tissues enhancedwith an optical contrast agent. *Opt. Lett.* **30**, 507–509 (2005).
19. Zhang, Y., Hong, H. & Cai, W. Photoacoustic Imaging. *Cold Spring Harbor Protocols* **2011**, pdb.top065508 (2011).
20. Yang, X., Skrabalak, S. E., Li, Z.-Y., Xia, Y. & Wang, L. V. Photoacoustic Tomography of a Rat Cerebral Cortex in vivo with Au Nanocages as an Optical Contrast Agent. *Nano Lett* **7**, 3798–3802 (2007).
21. Song, K. H., Kim, C., Cobley, C. M., Xia, Y. & Wang, L. V. Near-infrared gold nanocages as a new class of tracers for photoacoustic sentinel lymph node mapping on a rat model. *Nano Lett* **9**, 183–188 (2008).
22. Shashkov, E. V., Everts, M., Galanzha, E. I. & Zharov, V. P. Quantum dots as multimodal photoacoustic and photothermal contrast agents. *Nano Lett* **8**, 3953–3958 (2008).
23. Pu, K. *et al.* Semiconducting polymer nanoparticles as photoacoustic molecular imaging probes in living mice. *Nat Nanotechnol* **9**, 233–239 (2014).
24. Krumholz, A., Shcherbakova, D. M., Xia, J., Wang, L. V. & Verkhusha, V. V. Multicontrast photoacoustic in vivo imaging using near-infrared fluorescent proteins. *Sci Rep* **4**, 3939 (2014).
25. Tan, M. C., Naczynski, D. J., Moghe, P. V. & Riman, R. E. Engineering the design of brightly-emitting luminescent nanostructured photonic composite systems. *Aust J Chem* **66**, 1008–1020 (2013).
26. Yuan, D., Tan, M. C., Riman, R. E. & Chow, G. M. Comprehensive study on the size effects of the optical properties of $NaYF_4$:Yb,Er nanocrystals. *J Phys Chem C* **117**, 13297–13304 (2013).
27. van Saders, B., Al-Baroudi, L., Tan, M. C. & Riman, R. E. Rare-earth doped particles with tunable infrared emissions for biomedical imaging. *Opt Mater Express* **3**, 566–573 (2013).
28. Wang, F. & Liu, X. Recent advances in the chemistry of lanthanide-doped upconversion nanocrystals. *Chem Soc Rev* **38**, 976–989 (2009).
29. Pratx, G., Carpenter, C. M., Sun, C. & Xing, L. X-ray luminescence computed tomography via selective excitation: a feasibility study. *IEEE Trans Med Imaging* **29**, 1992–1999 (2010).
30. Zeng, S., Tsang, M.-K., Chan, C.-F., Wong, K.-L. & Hao, J. PEG modified $BaGdF_5$:Yb/Er nanoprobes for multi-modal upconversion fluorescent, in vivo X-ray computed tomography and biomagnetic imaging. *Biomaterials* **33**, 9232–9238 (2012).
31. Liu, J.-n. *et al.* Simultaneous nuclear imaging and intranuclear drug delivery by nuclear-targeted multifunctional upconversion nanoprobes. *Biomaterials* **33**, 7282–7290 (2012).
32. Xing, H. *et al.* Multifunctional nanoprobes for upconversion fluorescence, MR and CT trimodal imaging. *Biomaterials* **33**, 1079–1089 (2012).
33. Lee, J. *et al.* RGD peptide-conjugated multimodal $NaGdF_4$:Yb^{3+}/Er^{3+} nanophosphors for upconversion luminescence, MR, and PET imaging of tumor angiogenesis. *J Nucl Med* **54**, 96–103 (2013).
34. Zhou, J. *et al.* Fluorine-18-labeled Gd^{3+}/Yb^{3+}/Er^{3+} co-doped $NaYF_4$ nanophosphors for multimodality PET/MR/UCL imaging. *Biomaterials* **32**, 1148–1156 (2011).
35. Cheng, L., Wang, C. & Liu, Z. Upconversion nanoparticles and their composite nanostructures for biomedical imaging and cancer therapy. *Nanoscale* **5**, 23–37 (2013).
36. Zhang, F. *et al.* Uniform nanostructured arrays of sodium rare-earth fluorides for highly efficient multicolor upconversion luminescence. *Angew Chem Int Ed* **46**, 7976–7979 (2007).
37. Wang, L. & Li, Y. Controlled synthesis and luminescence of lanthanide doped $NaYF_4$ nanocrystals. *Chem Mater* **19**, 727–734 (2007).
38. Tan, M. C., Al-Baroudi, L. & Riman, R. E. Surfactant effects on efficiency enhancement of infrared-to-visible upconversion emissions of $NaYF_4$:Yb-Er. *ACS Appl Mater Interfaces* **3**, 3910–3915 (2011).
39. Todorović, D. M., Nikolić, P. M. & Ristovski, Z. D. in *Physical Acoustics* (eds Oswald Leroy & MackA Breazeale) [Ch. 87], [641–646] (Springer US, 1991).
40. Tan, M. C., Connolly, J. & Riman, R. E. Optical Efficiency of Short Wave Infrared Emitting Phosphors. *J Phys Chem C* **115**, 17952–17957 (2011).
41. El-Agmy, R., Al-Hosiny, N., Abdallah, S. & Abdel-Aal, M. Generation of Short Wavelength in Up-Conversion of Tm^{+3} Doped Fluoride Glass and Its Application in Fiber Lasers. *J Mod Phys* **5**, 123–127 (2014).
42. Liao, L. D. *et al.* Investigation of the cerebral hemodynamic response function in single blood vessels by functional photoacoustic microscopy. *J Biomed Opt* **17**, 061210 (2012).
43. Liao, L. D. *et al.* Imaging brain hemodynamic changes during rat forepaw electrical stimulation using functional photoacoustic microscopy. *Neuroimage* **52**, 562–570 (2010).

Acknowledgments

MC Tan and Y Sheng would like to gratefully acknowledge the funding support from the Singapore University of Technology and Design (SUTD) Start-up Research Grant and the

SUTD-MIT International Design Center. MC Tan and Y Sheng would like to thank D Yuan, Edinburgh Instruments and Bruker AXS for their assistance in making the absorption, decay time and powder XRD measurements, respectively. L-D Liao and N Thakor also would like to thank the National University of Singapore for supporting the Neurovascular Imaging Laboratory (NIL) at the Singapore Institute for Neurotechnology (SiNAPSE) under grant number R-711-000-026-133.

Author contributions

Y.S., M.C.T., L.D.L. and N.T. conceived the study and designed the experiments. Y.S. performed the experiments to synthesize and characterize the materials. L.D.L. performed the PA signal measurements and imaging. Y.S., M.C.T. and L.D.L. discussed and analyzed the data. Y.S., M.C.T., L.D.L. and N.T. wrote and revised the manuscript.

Additional information

Supplementary information accompanies this paper at http://www.nature.com/scientificreports

Competing financial interests: The authors declare no competing financial interests.

How to cite this article: Sheng, Y., De Liao, L.-D., Thakor, N. & Tan, M.C. Rare-Earth Doped Particles as Dual-Modality Contrast Agent for Minimally-Invasive Luminescence and Dual-Wavelength Photoacoustic Imaging. *Sci. Rep.* **4**, 6562; DOI:10.1038/srep06562 (2014).